RESEARCH ARTICLE
Journal Section

Evaluating Different Approaches for Modelling Rotor Aero-servo-dynamics in Frequency-Domain Analysis of Floating Wind Turbines

Serag-Eldin Abdelmoteleb[1] | **Erin E. Bachynski-Polić**[1]

[1]Department of Marine Technology, NTNU, Trondheim, 7050, Norway

Correspondence
Serag-Eldin Abdelmoteleb, Department of Marine Technology, NTNU, Trondheim, 7050, Norway
Email: serageldin.abdelmoteleb@ntnu.no

Funding information
Research Council of Norway, ENERGIX, Grant/Award number: 308839

Computationally efficient frequency-domain models can play a very important role in facilitating conceptual design optimization of floating wind turbines (FWTs). However, achieving sufficient accuracy in such models is challenging due to the nonlinear variation of the aerodynamic loads, particularly the interaction between the floating platform motions and the controller. Building on previously proposed approaches from the literature, this work implements and improves upon three methods to evaluate the influence of rotor dynamics on FWTs dynamics in frequency domain. The investigated methods rely on: coupled fixed-nacelle simulations in turbulent wind; decay tests in steady wind; and linearized analytical expressions of the steady state aerodynamic loads. The main objective is to assess the suitability of these methods for future optimization of the floating platform and the mooring system. The various techniques are compared through a case study of three semi-submersible FWTs with increasing rotor size. While all approaches have good accuracy below-rated wind speed, only the decay test approach provide good estimates of the wind-induced global responses across all tested conditions.

KEYWORDS
Floating wind turbines, Frequency-domain, Aerodynamic damping

1 | INTRODUCTION

The need to reduce the levelized cost of energy of floating wind turbines (FWTs) has spurred interest in computationally efficient frequency-domain models of FWTs. These models are crucial for the conceptual design optimization of the various components of FWTs such as the substructure, mooring system and tower. One of the main challenges when modelling FWT dynamics in frequency domain is to accurately capture the aerodynamic loads, including the interaction between rotor dynamics and the motions of the FWT. This interaction, which is governed by the controller, can introduce both damping and inertial/stiffness effects. These effects have been reported experimentally [1, 2], and investigated numerically [3]. Various approaches have been implemented in previous studies to model these effects in frequency-domain analysis of FWTs. Generally, these approaches can be split into two categories, namely, system identification and linearization.

System identification approaches make use of coupled time-domain aero-hydro-servo-elastic simulations to obtain aerodynamic added mass, damping, and excitation coefficients corresponding to the degrees of freedom (DOFs) of interest. One way of doing this is to evaluate the transfer function between wind speed and thrust force from time-domain simulations of a fixed nacelle in turbulent wind. This transfer function can then be used to model aerodynamic excitation [4, 5]. Coupled simulations in steady wind have also been used to obtain aerodynamic damping coefficients. This could be achieved either through decay tests of the platform's motions [6] or forced oscillations of the nacelle [5]. Decay tests require prior information about the platform and mooring system designs, which makes them inconvenient for design optimization of these components. Additionally, inertial effects resulting from the motion-controller interaction, which can have significant effects, especially for pitch motion [3], are not captured by this approach as implemented in the literature. On the other hand, using forced nacelle oscillations in steady wind, both damping and inertial effects can be captured with no prior information about the support system, as long as the oscillation frequencies cover the range in which the natural frequencies of the DOFs of interest reside. Nevertheless, the underlying assumption of harmonic oscillation of the aerodynamic loads can introduce significant inaccuracies in regions with strong nonlinearities, such as operation near rated wind speed.

In general, system identification approaches can be useful for designing the support system components for a given rotor design. However, they are unfit for a holistic design optimization, which includes parameters related to rotor or controller designs. For this purpose, linearization approaches offer a promising alternative. These approaches are based on using the derivatives of the aerodynamic loads obtained from steady state simulations using blade element momentum (BEM) method to linearize the aerodynamic loads around the steady state operation point. The simplest way to achieve this is to use the derivative of the steady state thrust curve of the rotor with respect to wind speed as both the excitation and damping terms in the FWT's equation of motion [4, 7]. This approach can be useful to estimate the dynamic response of FWTs at high frequencies of oscillation which are far from the controller frequencies and thus are not significantly influenced by controller action. However, this method is not adequate for obtaining the low frequency FWT response, as it does not account for the frequency-dependence of the aerodynamic coefficients introduced by the controller [5]. Silva de Souza et al. [5] proposed a more elaborate approach to obtain the frequency-dependent aerodynamic added mass and damping coefficients. They used Taylor series expansion to obtain linearized expressions for the aerodynamic thrust and torque around the steady state operation point. These expressions were then combined with the rotor dynamics equation, which includes the generator torque and blade pitch controller effects, to derive analytical expressions of the aerodynamic added mass and damping coefficients. The method was later extended by Hall et al. [8] to include aerodynamic excitation as well as the effect of nacelle velocity feedback on the blade pitch controller. While this approach can capture some controller effects such as generator torque and blade pitch variation in the below-rated and above-rated control regions, other significant aspects of controller action such as saturation and switching between control regions are not accounted for.

All the aforementioned methods include the effects of the rotor and controller dynamics implicitly by adding extra inertia and damping coefficients to the FWT dynamics. Alternatively, rotor and controller dynamics can be explicitly included as additional DOFs in the frequency-domain model and coupled to the FWT degrees of freedom. This allows for employing statistical linearization techniques to improve the accuracy of the frequency-domain model. These techniques rely on estimating the response of a nonlinear system using an equivalent linear system with dynamic coefficients that depend on the response statistics, assuming they can be approximated by a joint Gaussian probability distribution function of the system's states. The responses are found iteratively by updating the system's dynamic coefficients based on response statistics until convergence criteria are met. Lupton et al. implemented this approach to estimate blade aeroelastic responses [9] and global motion responses [10] for 5 MW FWTs subject to harmonically varying wind speed. The method provided good estimates away from rated wind speed compared to coupled time-domain simulations. The poor performance near rated wind speeds was attributed to the nonlinear controller behavior, as well as the generator torque and blade pitch controller interaction. A more general implementation of statistical linearization was presented by da Silva et al. [11, 12] who used stochastic linearization to estimate the responses of 5 MW FWTs in turbulent wind conditions. They found good agreement of the estimated surge and pitch responses obtained from the linearized model and coupled time-domain simulations. However, these studies excluded near-rated conditions due to the non-Gaussian nature of the responses in this region caused by the transition between the generator torque and blade pitch controllers.

The main motivation that prompted the investigation presented herein is the need for a realistic mooring design for the 25MW FWTs presented in a previous study [13]. Consequently, the current work focuses on the aforementioned implicit modeling approaches of rotor dynamics to avoid the computational overhead introduced by solving the dynamics of the rotor and controller. Solving these extra DOFs can make the frequency-domain analysis an order of magnitude slower if an iterative approach is implemented [10]. The study will explore various methods of modelling rotor aero-servo dynamics in frequency-domain simulations and try to address their shortcomings. The aim is to find the most suitable method to be used for the optimization of the FWT support system components for given rotor and controller designs. Three designs of semi-submersible FWTs with power ratings of 5, 15 and 25 MW will be used as case studies to evaluate the different modelling techniques. The FWT frequency-domain model and the methods for obtaining the aerodynamic coefficients employed in this work are described in Section 2. The case study and its results and findings are presented in Section 3. Finally, conclusions and recommendations are given in Section 4.

2 | FREQUENCY DOMAIN MODELLING

This section gives a brief overview of how the low frequency dynamics of FWTs are modeled in frequency-domain. Next, the methods used to obtain the aerodynamic coefficients in this study are described.

2.1 | Low frequency dynamics of FWTs

The frequency-dependent complex amplitudes of the rigid body motions $\hat{\eta}(\omega)$ of a FWT subject to low-frequency wind excitation $\hat{\mathbf{F}}_{aero}(\omega)$ are obtained by solving the following equation of motion in the frequency domain:

$$[-\omega^2(\mathbf{M}+\mathbf{A}_0+\mathbf{A}_{aero}(\omega))+i\omega(\mathbf{B}_{lin}+\mathbf{B}_{aero}(\omega))+\mathbf{K}_{hs}+\mathbf{K}_m]\hat{\eta}(\omega)(\omega)=\hat{\mathbf{F}}_{aero}(\omega) \tag{1}$$

where $\mathbf{M}$ is the mass matrix of the FWT. For low-frequency platform motions, the hydrodynamic radiation damping is negligible, and the radiation effects can be represented by the zero-frequency added mass matrix $\mathbf{A}_0$. $\mathbf{B}_{lin}$ is a linearized damping matrix that represents viscous damping of the platform and tower. $\mathbf{A}_{aero}(\omega)$ and $\mathbf{B}_{aero}(\omega)$ are the linear frequency-dependent aerodynamic added mass and damping matrices, respectively. $\mathbf{K}_{hs}$ and $\mathbf{K}_m$ are the

hydrostatic and mooring stiffness matrices, respectively. The mooring stiffness matrix is linearized about the mean position, evaluated from solving static equilibrium under mean aerodynamic loads at a given mean wind speed.

The vector or complex response amplitude operators (RAOs) relating the rigid body motion amplitudes to wind speed turbulence amplitudes $\hat{U}(\omega)$ is thus given by:

$$\mathbf{RAO}(\omega) = \frac{\hat{\eta}(\omega)}{\hat{U}(\omega)} = \mathbf{H}_{F\eta}(\omega)\hat{\mathbf{f}}_{aero}(\omega) \tag{2}$$

where $\mathbf{f}_{aero}(\omega)$ contains the aerodynamic loads per unit wind speed turbulence amplitude and $\mathbf{H}_{F\eta}$ is the load-to-response transfer function matrix given as:

$$\mathbf{H}_{F\eta}(\omega) = [-\omega^2(\mathbf{M} + \mathbf{A}_0 + \mathbf{A}_{aero}(\omega)) + i\omega(\mathbf{B}_{lin} + \mathbf{B}_{aero}(\omega)) + \mathbf{K}_{hs} + \mathbf{K}_m]^{-1}. \tag{3}$$

The motion response spectra $\mathbf{S}_{\eta\eta}(\omega)$ can then be obtained from:

$$\mathbf{S}_{\eta\eta}(\omega) = \left|\mathbf{RAO}(\omega)\right|^2 S_{UU}(\omega) \tag{4}$$

where $S_{UU}(\omega)$ is the rotor-averaged wind speed spectrum. The motion response variance vector σ^2 can thus be obtained from:

$$\sigma^2 = \int_0^\infty \mathbf{S}_{\eta\eta}(\omega)\, d\omega \tag{5}$$

The rest of this section illustrates the different methods used in this study to evaluate $\hat{\mathbf{f}}_{aero}(\omega)$, $\mathbf{A}_{aero}(\omega)$, and $\mathbf{B}_{aero}(\omega)$. For simplicity, only planar rigid body motions, namely surge (η_1), heave (η_3), and pitch (η_5), are considered in this study as illustrated in Figure 1. However, the methods presented in this work could be extended to include more DOFs.

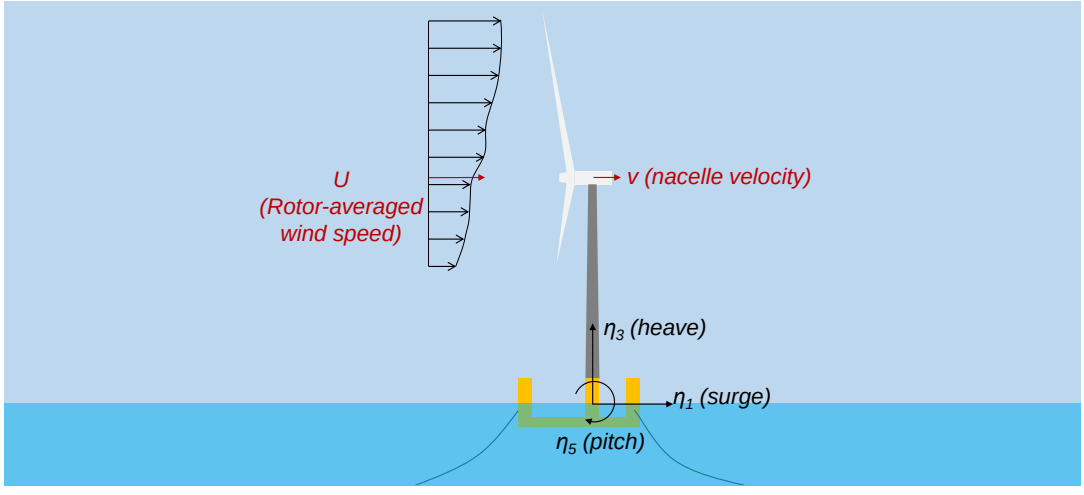

FIGURE 1 Definitions of planar wind-induced rigid body motions for a floating wind turbine

2.2 | Method 1: Using fixed nacelle in turbulent wind simulations

Coupled time-domain simulations of a wind turbine with fixed nacelle in turbulent wind with only the rotor and controller DOFs active can be used to obtain a transfer function between rotor-averaged wind speed and aerodynamic thrust [4, 5]. For a given mean wind speed $\overline{U}$, this transfer function is given by:

$$H_{UT}(\overline{U},\omega) = \sqrt{\frac{S_{TT}(\overline{U},\omega)}{S_{UU}(\overline{U},\omega)}} \quad , \qquad S_{UU}(\overline{U},\omega) > 0 \tag{6}$$

where U and T are the rotor-averaged horizontal wind speed and aerodynamic thrust, respectively. S_{UU} and S_{TT} are the corresponding power spectral densities (PSDs) of U and T, respectively. To obtain H_{UT}, the coupled model is run with multiple realizations of the turbulent wind field for a given mean wind speed. The resulting time series of U and T from all simulations are combined to form ensembles from which S_{UU} and S_{TT} can be obtained. This is repeated at different mean wind speeds to cover the region of interest, resulting in a 2D grid of values of H_{UT} as a function of mean wind speed and frequency. This grid is used as a look-up table to obtain the aerodynamic excitation per unit wind turbulence amplitude introduced in Equation (2) as follows:

$$\hat{\mathbf{f}}_{aero}(\overline{U},\omega) = H_{UT}(\overline{U},\omega)\begin{pmatrix} 1 \\ 0 \\ h_{hub} \end{pmatrix} \tag{7}$$

where h_{hub} is the hub height. The transfer function in Equation (6) is real-valued, i.e., it only provides information about the amplitude gain but not the phase difference between wind speed and thrust. Phase information can be extracted from these simulations by evaluating the first-order transfer function as follows:

$$H_{UT}^{(1)}(\overline{U},\omega) = \frac{S_{UT}(\overline{U},\omega)}{S_{UU}(\overline{U},\omega)} \quad , \qquad S_{UU}(\overline{U},\omega) > 0 \tag{8}$$

where S_{UT} is the cross-spectral density (CSD) between rotor-averaged wind speed and thrust. This transfer function is complex-valued, including both gain and phase information. This allows the evaluation of the aerodynamic added mass and damping coefficient matrices in Equation (1) from the imaginary and real parts of the first-order transfer function by using turbulence as a proxy for the horizontal motion of the nacelle.

$$\mathbf{A}_{aero}(\overline{U},\omega) = \Im\{H_{UT}^{(1)}(\overline{U},\omega)\}/\omega \begin{bmatrix} 1 & 0 & h_{hub} \\ 0 & 0 & 0 \\ h_{hub} & 0 & h_{hub}^2 \end{bmatrix} \quad , \quad \mathbf{B}_{aero}(\overline{U},\omega) = \Re\{H_{UT}^{(1)}(\overline{U},\omega)\} \begin{bmatrix} 1 & 0 & h_{hub} \\ 0 & 0 & 0 \\ h_{hub} & 0 & h_{hub}^2 \end{bmatrix} \tag{9}$$

It should be noted that the gains of the transfer function obtained from Equation (6) are equivalent to those obtained from Equation (8) only if the system is linear. Thus, using the former to model aerodynamic excitation includes higher-order effects within the wind excitation frequency range. Consequently, Equation (6) is used to model aerodynamic excitation for all system identification techniques employed in this study.

2.3 | Method 2: Using decay tests in steady wind simulations

Using decay tests in steady wind to obtain aerodynamic damping of FWTs was proposed by Pegalajar-Jurado et al. [6]. The aim of this approach is to find an equivalent linear damping that delivers the same work done by aerodynamic damping per oscillation cycle of the DOF of interest. For a given mean wind speed, this is achieved by performing a decay test for said DOF in steady wind while the turbine is operating with an active controller and all other DOFs are fixed. If all damping sources, such as hydrodynamic or structural damping, are disabled, then the damping ratio could be extracted from the decay time series and subsequently the aerodynamic damping for the DOF of interest can be evaluated given its inertia and stiffness properties. This is repeated for multiple wind speeds covering the range of operation, thus giving the aerodynamic damping as a function of mean wind speed. As pointed out in the introduction, this approach has two main limitations: it requires prior knowledge of the support system design (e.g., platform and mooring designs); and it does not account for the inertial effects of the controller, which can have significant impact on the motion responses in some situations, such as pitch motions in above-rated conditions [3]. The following is a modification of this method to address these limitations.

To eliminate the need for prior knowledge of the support system design, the floating support structure is replaced in the simulations by an equivalent single DOF system. This single DOF system is defined to have a mass m_{eq} and a stiffness k_{eq}, which are chosen to achieve a desired natural frequency ω_n and critical damping $b_{c,eq}$ as follows:

$$m_{eq} = \frac{b_{c,eq}}{2\omega_n} \quad , \quad k_{eq} = \omega_n^2 m_{eq}. \tag{10}$$

No hydrodynamic or mechanical damping is modeled for the single DOF system, such that the only damping source is the aerodynamic damping $b_{aero,i}$, such that:

$$b_{aero,i} = 2\zeta_{eq}\sqrt{k_{eq} m_{eq}} \tag{11}$$

where ζ_{eq} is the equivalent system's damping ratio. If no information is available on the support system design, ω_n can be substituted by the variable oscillation frequency ω, which covers the frequency range in which the natural frequency of η_i is expected to lie. This is achieved by varying m_{eq} and k_{eq} to obtain single DOF systems that would naturally oscillate at the desired frequencies. The aerodynamic damping as a function of mean wind speed and oscillation frequency is then found by performing decay tests for the equivalent system for the ranges of interest of mean wind speeds and oscillation frequencies. For a semi-submersible FWT, a frequency range of 0.005 to 0.05 Hz would be sufficient to capture both surge and pitch natural frequencies. Additionally, setting $b_{c,eq}$ to a high value relative to the expected aerodynamic damping ensures that the equivalent system has a low damping ratio, thus avoiding situations with large damping ratios which can make it difficult to capture peaks in the time series, and also allows easier identification of the aerodynamic added mass. For surge, an appropriate estimate of the aerodynamic damping is the slope of the steady state thrust curve. Thus, setting the critical damping to 50 times the maximum slope of the steady state thrust curve will result in damping ratio values of around 2% for surge. A similar approach was used to choose the critical damping for pitch.

For each combination of mean wind speed and oscillation frequency, a decay test is carried out for the DOF of interest. The damping ratio ζ_{eq} and damped frequency ω_d of the equivalent system can be extracted from the decay test time series using the average logarithmic decrement and average peak to peak period, respectively. The natural frequency of the equivalent system ω_{eq}, aerodynamic added mass and damping for the i^{th} DOF can then be evaluated from the expressions in Equations (12) to (14).

$$\omega_{eq}(\overline{U},\omega) = \frac{\omega_d(\overline{U},\omega)}{\sqrt{1-\zeta_{eq}^2(\overline{U},\omega)}} \tag{12}$$

$$a_{aero,i}(\overline{U},\omega) = \frac{k_{eq}(\omega)}{\omega_{eq}^2(\overline{U},\omega)} - m_{eq}(\omega) \tag{13}$$

$$b_{aero,i}(\overline{U},\omega) = 2\zeta_{eq}(\overline{U},\omega)\sqrt{\left(m_{eq}(\omega)+a_{aero,i}(\overline{U},\omega)\right)k_{eq}(\omega)} \tag{14}$$

This procedure is used to evaluate the aerodynamic added mass and damping for all combinations of mean wind speeds and oscillation frequencies under consideration and for all DOFs of interest. This results in grids which can be used as look-up tables in the frequency-domain model to interpolate the values of diagonal terms in the aerodynamic added mass and damping matrices. The effect of coupling between surge and pitch might be significant, especially for larger turbine sizes with large hub heights and low pitch natural frequencies. This can be accounted for as follows:

$$\mathbf{A}_{aero}(\overline{U},\omega) = \begin{bmatrix} a_{aero,1}(\overline{U},\omega) & 0 & a_{aero,5}(\overline{U},\omega)/h_{hub} \\ 0 & 0 & 0 \\ a_{aero,1}(\overline{U},\omega)h_{hub} & 0 & a_{aero,5}(\overline{U},\omega) \end{bmatrix} \tag{15}$$

$$\mathbf{B}_{aero}(\overline{U},\omega) = \begin{bmatrix} b_{aero,1}(\overline{U},\omega) & 0 & b_{aero,5}(\overline{U},\omega)/h_{hub} \\ 0 & 0 & 0 \\ b_{aero,1}(\overline{U},\omega)h_{hub} & 0 & b_{aero,5}(\overline{U},\omega) \end{bmatrix} \tag{16}$$

2.4 | Method 3: Linearized analytical expressions

Analytical expressions for aerodynamic coefficients based on Taylor-series expansion of aerodynamic thrust and torque were derived by Silva de Souza et al. [5]. This approach relies on relating aerodynamic thrust to horizontal nacelle velocity to obtain aerodynamic added mass and damping coefficients, taking into account the influence of the blade pitch controller. Hall et al. [8] later extended these expressions to include turbulent wind excitation, as well as the effects of the generator torque controller and nacelle velocity feedback. The following derivation builds on this work and introduces some modifications to the expressions.

The aerodynamic loads depend on rotor-averaged wind speed U, nacelle velocity v, rotor speed Ω, and blade pitch angle β. Thus, linear expressions for thrust and torque variation about a mean operation point can be obtained by using Taylor-series expansion and ignoring higher order terms, as follows:

$$T(t) = \bar{T} + \delta T(t) = \bar{T} + \frac{\partial T}{\partial U}\Big|_{\overline{U}}(\delta U(t) - v(t)) + \frac{\partial T}{\partial \Omega}\Big|_{\overline{U}}\delta\Omega(t) + \frac{\partial T}{\partial \beta}\Big|_{\overline{U}}\delta\beta(t) \tag{17}$$

$$Q(t) = \bar{Q} + \delta Q(t) = \bar{Q} + \frac{\partial Q}{\partial U}\Big|_{\overline{U}}(\delta U(t) - v(t)) + \frac{\partial Q}{\partial \Omega}\Big|_{\overline{U}}\delta\Omega(t) + \frac{\partial Q}{\partial \beta}\Big|_{\overline{U}}\delta\beta(t) \tag{18}$$

where t is time, the over bar denotes mean values, and δ denotes variation around the mean value. The mean values and partial derivatives of the aerodynamic loads at a given operational mean wind speed can be obtained from steady state BEM analysis. Rotor speed dynamics can be modelled using the following single DOF equation of motion:

$$J\dot{\Omega}(t) = Q(t) - N_g\tau_g(t) \tag{19}$$

where $\dot{\Omega}$ is the rotor rotational acceleration, J is the rotor and drivetrain moment of inertia about the low-speed shaft's axis, N_g is the gear ratio, and τ_g is the generator torque. By substituting the linearized aerodynamic torque in Equation (18) into Equation (19), and assuming that the mean aerodynamic and generator torques are in equilibrium, the rotor speed dynamics equation becomes:

$$J\dot{\Omega}(t) = \frac{\partial Q}{\partial U}\Big|_{\bar{U}}(\delta U(t) - v(t)) + \frac{\partial Q}{\partial \Omega}\Big|_{\bar{U}}\delta\Omega(t) + \frac{\partial Q}{\partial \beta}\Big|_{\bar{U}}\delta\beta(t) - N_g\delta\tau_g(t) \tag{20}$$

The variations of the generator torque and blade pitch are governed by the controllers. The ROSCO controller [14] is used as a reference controller in this work. For below-rated wind speeds, ROSCO implements one of two strategies, either tip speed ratio (TSR) tracking PI control or the traditional $K\Omega^2$ law. For the TSR tracking PI controller, the generator torque is given by:

$$\tau_g(t) = k_{P\tau}\left(\Omega(t) - \Omega_{ref}(t)\right) + k_{I\tau}\int_0^t \left(\Omega(\mu) - \Omega_{ref}(\mu)\right)d\mu \tag{21}$$

where $k_{P\tau}$ and $k_{I\tau}$ are the proportional and integral gains of the generator torque controller, respectively. Ω_{ref} is the reference rotor speed, which is determined based on relative wind speed to achieve a constant TSR as follows:

$$\Omega_{ref}(t) = \frac{\lambda\left(U(t) - v(t)\right)}{R} = \frac{\lambda\left(\bar{U} + \delta U(t) - v(t)\right)}{R} \tag{22}$$

where λ is the TSR and R is the rotor radius. Hence, the variation of the generator torque around the mean becomes:

$$\delta\tau_g(t) = k_{P\tau}\left(\delta\Omega(t) - \frac{\lambda(\delta U(t) - v(t))}{R}\right) + k_{I\tau}\int_0^t\left(\delta\Omega(\mu) - \frac{\lambda(\delta U(\mu) - v(\mu))}{R}\right)d\mu \tag{23}$$

If the $K\Omega^2$ law is implemented, then the generator torque is given by:

$$\tau_g(t) = K\Omega_g(t)^2 = KN_g^2\Omega(t)^2, \qquad \text{where} \qquad K = \frac{\pi\rho_{air}R^5C_{p,max}}{2\lambda_{opt}^3N_g^3\eta_{gb}} \tag{24}$$

where Ω_g is the generator speed, ρ_{air} is air density, $C_{p,max}$ maximum power coefficient, λ_{opt} is the optimal TSR, and η_{gb} is the gearbox efficiency. In this case, assuming the variation of rotor speed is small compared to the mean rotor speed, the variation of generator torque becomes:

$$\delta\tau_g(t) \approx 2KN_g^2\bar{\Omega}\delta\Omega(t) \tag{25}$$

Equation (25) is a special case of Equation (23) where $k_{P\tau} = 2KN_g^2\bar{\Omega}$, $k_{I\tau} = 0$ and the TSR terms are dropped.

The variation of the collective blade pitch angle is governed by a PI controller, as given below:

$$\delta\beta(t) = k_{P\beta}\delta\Omega(t) + k_{I\beta}\int_0^t \delta\Omega(\mu)d\mu + \beta_f(t) \tag{26}$$

where $k_{P\beta}$ and $k_{I\beta}$ are the proportional and integral gains of the blade pitch controller, respectively. For the blade pitch controller, $\delta\Omega$ is the deviation of Ω from the rated rotor speed. β_f is an additional blade pitch command that depends on the feedback of the floating nacelle motion, which is implemented in ROSCO to reduce the need for detuning the blade pitch controller to avoid negative platform pitch damping. This floating feedback term can be proportional to either the translational or rotational velocity of the nacelle through a constant gain k_{ff}. The unit of this constant depends on which feedback signal is being used. For convenience, the floating feedback term is defined here directly in terms of surge and pitch velocities feedback signals as follows:

$$\beta_f(t) = k_{ff_1}\dot{\eta}_{1_f}(t) + k_{ff_5}\dot{\eta}_{5_f}(t) \tag{27}$$

where $k_{ff_1} = k_{ff}$ and $k_{ff_5} = k_{ff}h_{hub}$ if the nacelle's translational velocity is used as the floating feedback signal, while $k_{ff_1} = 0$ and $k_{ff_5} = k_{ff}$ if the nacelle's rotational velocity is used instead. Applying the recommended tuning procedure [14], ROSCO filters the nacelle velocity feedback using a first order high pass filter ($F_{HP}^{(1)}$) with a cutoff frequency of 0.01042 rad/s and a second order low pass ($F_{LP}^{(2)}$) at the pitch natural frequency with a damping ratio of 1. Consequently, $\dot{\eta}_{1_f}$ and $\dot{\eta}_{5_f}$ are defined as the filtered surge and pitch velocities signals, respectively. Thus, Equation (27) can be rewritten as:

$$\delta\beta(t) = k_{P\beta}\delta\Omega(t) + k_{I\beta}\int_0^t \delta\Omega(\mu)d\mu + k_{ff_1}\dot{\eta}_{1_f}(t) + k_{ff_5}\dot{\eta}_{5_f}(t) \tag{28}$$

Assuming the more general case of TSR tracking PI generator torque controller below rated, if the expressions given in Equations (23) and (28) are inserted into Equation (20), the nacelle velocity v is replaced with $\dot{\eta}_1 + h_{hub}\dot{\eta}_5$, and a Laplace transform is taken, Equation (20) can be written in the s-domain as:

$$\begin{aligned}
\left[s^2 J - s\left(\frac{\partial Q}{\partial\Omega}\Big|_{\overline{U}} + \frac{\partial Q}{\partial\beta}\Big|_{\overline{U}} k_{P\beta} - N_g k_{P\tau}\right) - \left(\frac{\partial Q}{\partial\beta}\Big|_{\overline{U}} k_{I\beta} - N_g k_{I\tau}\right)\right]\tilde{\Omega}(s) = \\
\left[s\left(\frac{\partial Q}{\partial U}\Big|_{\overline{U}} + N_g k_{P\tau}\lambda/R\right) + N_g k_{I\tau}\lambda/R\right]\tilde{U}(s) \\
+\left[s\left(\frac{\partial Q}{\partial\beta}\Big|_{\overline{U}} H_{\dot{\eta}_1\beta}(s) - \frac{\partial Q}{\partial U}\Big|_{\overline{U}} - N_g k_{P\tau}\lambda/R\right) - N_g k_{I\tau}\lambda/R\right]s\tilde{\eta}_1(s) \\
+\left[s\left(\frac{\partial Q}{\partial\beta}\Big|_{\overline{U}} H_{\dot{\eta}_5\beta}(s)/h_{hub} - \frac{\partial Q}{\partial U}\Big|_{\overline{U}} - N_g k_{P\tau}\lambda/R\right) - N_g k_{I\tau}\lambda/R\right]h_{hub}s\tilde{\eta}_5(s)
\end{aligned} \tag{29}$$

where s is the Laplace variable and tilde denotes the Laplace transform of a variable. $H_{\dot{\eta}_1\beta}$ and $H_{\dot{\eta}_5\beta}$ are transfer functions from surge and pitch velocities, respectively, to their contribution to the floating feedback blade pitch command given as:

$$H_{\dot{\eta}_1\beta} = k_{ff_1}F_{HP}^{(1)}(s)F_{LP}^{(2)}(s) \quad , \quad H_{\dot{\eta}_5\beta} = k_{ff_5}F_{HP}^{(1)}(s)F_{LP}^{(2)}(s) \tag{30}$$

From Equation (29) three transfer functions can be extracted, namely: wind speed-to-rotor speed $H_{U\Omega}$, surge velocity-to-rotor speed $H_{\dot{\eta}_1\Omega}$, and pitch velocity-to-rotor speed $H_{\dot{\eta}_5\Omega}$.

$$H_{U\Omega}(\overline{U},s) = \frac{s(\frac{\partial Q}{\partial U}\big|_{\overline{U}} + N_g k_{P\tau}\lambda/R) + N_g k_{I\tau}\lambda/R}{s^2 J - s(\frac{\partial Q}{\partial \Omega}\big|_{\overline{U}} + \frac{\partial Q}{\partial \beta}\big|_{\overline{U}} k_{P\beta} - N_g k_{P\tau}) - (\frac{\partial Q}{\partial \beta} k_{I\beta}\big|_{\overline{U}} - N_g k_{I\tau})} \tag{31}$$

$$H_{\dot{\eta}_1\Omega}(\overline{U},s) = \frac{s(\frac{\partial Q}{\partial \beta}\big|_{\overline{U}} H_{\dot{\eta}_1\beta}(s) - \frac{\partial Q}{\partial U}\big|_{\overline{U}} - N_g k_{P\tau}\lambda/R) - N_g k_{I\tau}\lambda/R}{s^2 J - s(\frac{\partial Q}{\partial \Omega}\big|_{\overline{U}} + \frac{\partial Q}{\partial \beta}\big|_{\overline{U}} k_{P\beta} - N_g k_{P\tau}) - (\frac{\partial Q}{\partial \beta}\big|_{\overline{U}} k_{I\beta} - N_g k_{I\tau})} \tag{32}$$

$$H_{\dot{\eta}_5\Omega}(\overline{U},s) = \frac{s(\frac{\partial Q}{\partial \beta}\big|_{\overline{U}} H_{\dot{\eta}_5\beta}(s)/h_{hub} - \frac{\partial Q}{\partial U}\big|_{\overline{U}} - N_g k_{P\tau}\lambda/R) - N_g k_{I\tau}\lambda/R}{s^2 J - s(\frac{\partial Q}{\partial \Omega}\big|_{\overline{U}} + \frac{\partial Q}{\partial \beta}\big|_{\overline{U}} k_{P\beta} - N_g k_{P\tau}) - (\frac{\partial Q}{\partial \beta}\big|_{\overline{U}} k_{I\beta} - N_g k_{I\tau})} \times h_{hub} \tag{33}$$

Equations (31) to (33) indicate the dependence of the transfer functions on the mean wind speed $\overline{U}$. This dependence stems from the dependence of the aerodynamic derivatives on $\overline{U}$. Thus, rotor speed variation at a given mean wind speed can be represented in s-domain as:

$$\tilde{\Omega}(\overline{U},s) = H_{U\Omega}(\overline{U},s)\tilde{U}(s) + H_{\dot{\eta}_1\Omega}(\overline{U},s)s\tilde{\eta}_1(s) + H_{\dot{\eta}_5\Omega}(\overline{U},s)s\tilde{\eta}_5(s). \tag{34}$$

Substituting Equation (27) in Equation (17) and expanding v as before, the variation of thrust force in the s-domain can be represented as:

$$\begin{aligned}\tilde{T}(s) = {} & \frac{\partial T}{\partial U}\big|_{\overline{U}}\tilde{U}(s) \\ & + (\frac{\partial T}{\partial \beta}\big|_{\overline{U}} H_{\dot{\eta}_1\beta}(s) - \frac{\partial T}{\partial U}\big|_{\overline{U}})s\tilde{\eta}_1(s) \\ & + (\frac{\partial T}{\partial \beta}\big|_{\overline{U}} H_{\dot{\eta}_5\beta}(s)/h_{hub} - \frac{\partial T}{\partial U}\big|_{\overline{U}})sh_{hub}\tilde{\eta}_5(s) \\ & + (\frac{\partial T}{\partial \Omega}\big|_{\overline{U}} + \frac{\partial T}{\partial \beta}\big|_{\overline{U}} k_{P\beta} + \frac{1}{s}\frac{\partial T}{\partial \beta}\big|_{\overline{U}} k_{I\beta})\tilde{\Omega}(s).\end{aligned} \tag{35}$$

Inserting Equation (35) in Equation (34) and introducing mean wind speed dependence, Equation (35) becomes:

$$\tilde{T}(\overline{U},s) = H_{UT}(\overline{U},s)\tilde{U}(s) + H_{\dot{\eta}_1 T}(\overline{U},s)s\tilde{\eta}_1(s) + H_{\dot{\eta}_5 T}(\overline{U},s)s\tilde{\eta}_5(s) \tag{36}$$

where H_{UT}, $H_{\dot{\eta}_1 T}$, and $H_{\dot{\eta}_5 T}$ are transfer functions from wind speed, surge velocity, and pitch velocity to thrust, respectively, given by:

$$H_{UT}(\overline{U},s) = \frac{\partial T}{\partial U}\big|_{\overline{U}} + (\frac{\partial T}{\partial \Omega}\big|_{\overline{U}} + \frac{\partial T}{\partial \beta}\big|_{\overline{U}} k_{P\beta} + \frac{1}{s}\frac{\partial T}{\partial \beta}\big|_{\overline{U}} k_{I\beta})H_{U\Omega}(\overline{U},s) \tag{37}$$

$$H_{\dot{\eta}_1 T}(\overline{U},s) = \frac{\partial T}{\partial \beta}\big|_{\overline{U}} H_{\dot{\eta}_1\beta}(s) - \frac{\partial T}{\partial U}\big|_{\overline{U}} + (\frac{\partial T}{\partial \Omega}\big|_{\overline{U}} + \frac{\partial T}{\partial \beta}\big|_{\overline{U}} k_{P\beta} + \frac{1}{s}\frac{\partial T}{\partial \beta}\big|_{\overline{U}} k_{I\beta})H_{\dot{\eta}_1\Omega}(\overline{U},s). \tag{38}$$

$$H_{\dot{\eta}_5 T}(\overline{U}, s) = \frac{\partial T}{\partial \beta}\Big|_{\overline{U}} H_{\dot{\eta}_5 \beta}(s) - \frac{\partial T}{\partial U}\Big|_{\overline{U}} h_{hub} + \left(\frac{\partial T}{\partial \Omega}\Big|_{\overline{U}} + \frac{\partial T}{\partial \beta}\Big|_{\overline{U}} k_{P\beta} + \frac{1}{s}\frac{\partial T}{\partial \beta}\Big|_{\overline{U}} k_{I\beta}\right) H_{\dot{\eta}_5 \Omega}(\overline{U}, s). \tag{39}$$

By setting $s = i\omega$, the aerodynamic added mass and damping coefficients for surge and pitch can be evaluated from Equations (38) and (39) as follows:

$$a_{aero,1}(\overline{U}, \omega) = -\Re\{\frac{1}{i\omega} H_{\dot{\eta}_1 T}(\overline{U}, i\omega)\} \quad , \quad b_{aero,1}(\overline{U}, \omega) = -\Re\{\frac{1}{i\omega} H_{\dot{\eta}_1 T}(\overline{U}, i\omega)\} \tag{40}$$

$$a_{aero,5}(\overline{U}, \omega) = -\Re\{\frac{h_{hub}}{i\omega} H_{\dot{\eta}_5 T}(\overline{U}, i\omega)\} \quad , \quad b_{aero,5}(\overline{U}, \omega) = -\Re\{\frac{h_{hub}}{i\omega} H_{\dot{\eta}_5 T}(\overline{U}, i\omega)\} \tag{41}$$

The expressions in Equations (40) and (41) can be used to obtain the aerodynamic added mass and damping matrices in the same way as Equations (15) and (16). The frequency-dependent aerodynamic excitation per unit wind turbulence can be obtained similar to Equation (7) using the expression in Equation (37) by setting $s = i\omega$.

3 | CASE STUDY

To evaluate response estimates obtained via the methods outlined in the previous section, a case study of three FWTs operating in a water depth of 200 m is presented in this section. The three FWTs used in this case study are: the OC4 semi-submersible [15] supporting the NREL5MW wind turbine [16], the UMaine VolturnUS-S semi-submersible [17] supporting the IEA15MW wind turbine [18], and an upscaled version of the UMaine VolturnUS-S hosting a 25 MW wind turbine [13]. For the 15 MW FWT, the reference controller was used, and for the 5 and 25 MW FWTs, a ROSCO contoller was tuned based on the procedure presented by Abbas et al. [14]. The main properties of the reference FWTs and their controllers are summarized in Table 1.

TABLE 1 General properties of reference FWTs

Property	5 MW [15]	15 MW [17]	25 MW [13]
Total mass (t)	13518	20254	26419
Hub height (m)	90	150	193
Rotor radius (m)	63	120	154
Cut-in/ rated/ cut-out wind speed (m/s)	3.0/ 11.4/ 25.0	3.0/ 10.7/ 25.0	3.0/ 11.0/ 25.0
Rated rotor / generator speed (RPM)	12.1/ 1252	7.56/ 7.56	5.86/ 5.86
Surge/Pitch natural frequency at equilibrium (Hz)	0.009/ 0.040	0.007/ 0.036	0.008/ 0.024
Generator torque controller	$k\Omega^2$ law	PI TSR tracking	
Blade pitch controller	Detuned PI	Detuned PI + Nacelle rotational velocity feedback	
Blade pitch PI controller frequency (Hz)	0.032	0.032	0.022
Blade pitch saturation schedule	None	Minimum RPM + Peak shaving	Peak shaving
Mooring system type	3 studless chain catenary lines		
Fairlead/ anchor radius (m)	40.87/ 837.6	58.00/ 837.6	66.54/ 845.5
Line length (m)	835.4	850.0	850.0
Chain size (mm)	76.6	185.0	238.8

3.1 | Evaluation of aerodynamic coefficients

Based on the approaches outlined in section 2, three sets of simulations were performed to obtain the aerodynamic coefficients for the aforementioned reference FWTs, namely: turbulent wind simulations with a fixed nacelle; surge and pitch decay tests in steady wind; and steady-state BEM simulations. Both turbulent wind simulations and decay tests were performed using the coupled analysis tool OpenFAST version 3.1 [19]. For the steady-state simulations, the efficient BEM analysis tool CCBlade [20] was used.

Turbulent wind simulations with fixed nacelle were performed for a range of mean hub height wind speeds of 4 to 24 m/s with 2 m/s step, as well as 11 m/s (representing a condition near the rated speed). For each wind speed, 6 different realizations of turbulent wind fields were generated using TurbSim (an OpenFAST module) based on the Kaimal wind spectrum with IEC turbulence class B [21]. These realizations were used to run 1 hour coupled simulations (5400 s total simulation time with the first 1800 s removed to avoid transient effects). Ensembles of realizations of rotor-averaged wind speed and thrust force were used to obtain the spectra required for evaluating excitation, added mass, and damping coefficients as demonstrated in section 2.2. Figure 2 shows an example of the rotor-averaged wind speed PSD (S_{UU}), thrust PSD (S_{TT}), and the absolute value and phase angle of the CSD between rotor-averaged wind speed and thrust spectra (S_{UT}) for the IEA15MW wind turbine. At low below-rated wind speeds, thrust variation follows the rotor-averaged wind speed variation with a phase angle that is close to zero. This is because the generator torque is trying to maximize the generated power by tracking the optimum TSR based on the estimated wind speed. In contrast, the blade pitch controller tries to keep the rotor speed constant at its rated value at above-rated wind speeds. Consequently, thrust variations at low frequencies are reduced and the highly damped rotor dynamics due to the blade pitch PI controller results in an around 90 degrees phase angle between wind speed and thrust near the blade pitch controller's natural frequency of 0.032 Hz.

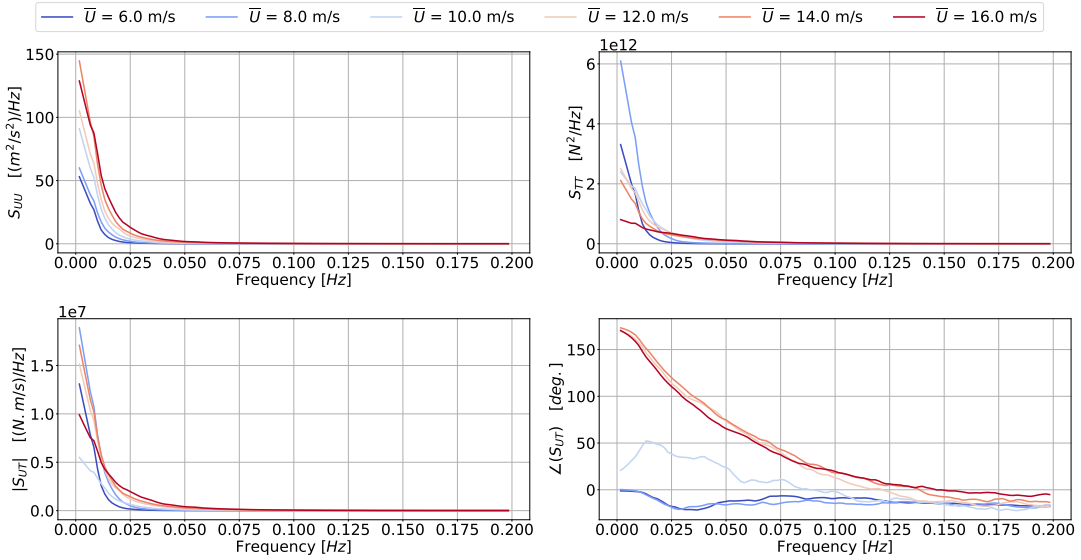

FIGURE 2 Spectra from turbulent wind simulations with fixed nacelle of the IEA15MW wind turbine: rotor-averaged wind speed PSD (S_{UU}), thrust PSD (S_{TT}), and the absolute value and phase angle of the CSD between rotor-averaged wind speed and thrust.

Surge and pitch decay test simulations in OpenFAST were carried out according to the procedure outlined in section 2.3 for each of the reference wind turbines. The decay tests were performed for 22 wind speeds ranging from 4 to 25 m/s with a step of 1 m/s, and 20 frequencies ranging from 0.005 Hz to 0.1 Hz with a step of 0.005 Hz, giving a total of 440 simulations for each of the surge and pitch DOFs for a single turbine. The platform's hydrostatic stiffness, added mass, and hydrodynamic damping (including radiation and quadratic damping) were set to zero. The tower is modelled as a massless rigid beam and the aerodynamic loads on it were disabled. The mooring system was not included in these simulations. All the DOFs were disabled, except for rotor rotation and a single platform DOF (surge or pitch). The platform's mass/ moment of inertia, and additional stiffness entries to OpenFAST's modules ElastoDyn and HydroDyn were used to tune the active platform DOF to have the desired oscillation frequency. Figure 3 shows examples of time series of decay tests for surge and pitch at oscillation frequencies of 0.01 Hz and 0.035 Hz, respectively, for the IEA15MW wind turbine, highlighting the peaks used to calculate the damping ratio.

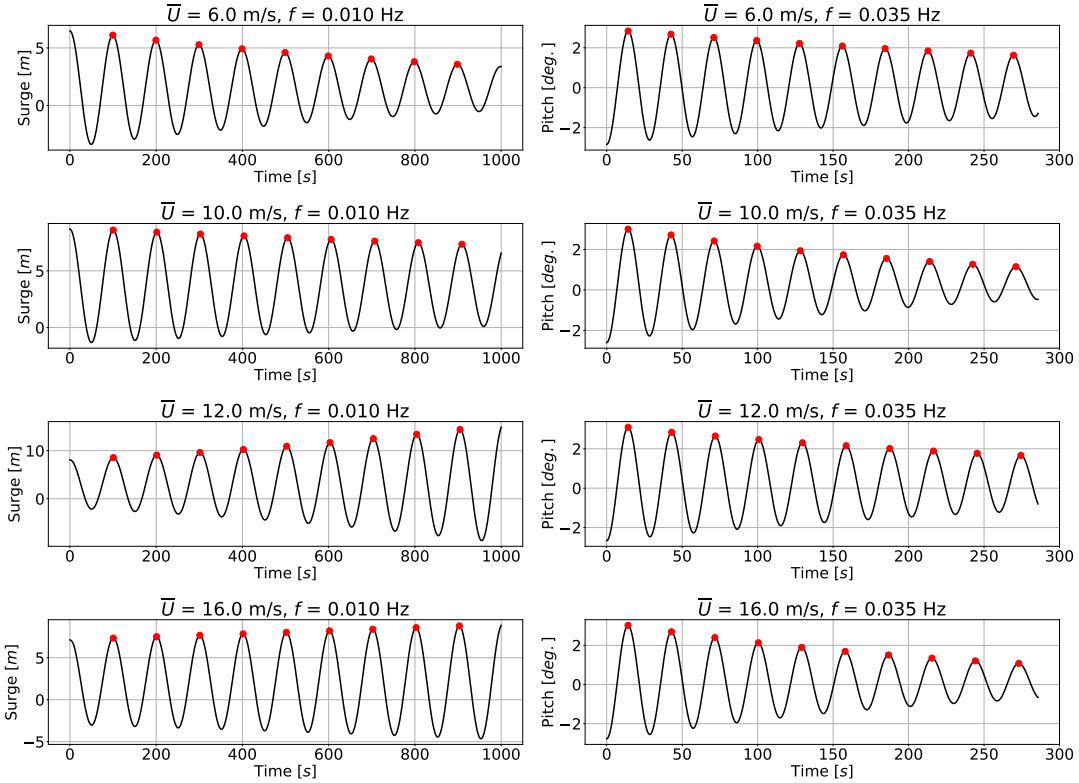

FIGURE 3 Examples of surge and pitch decay tests in steady wind for the IEA 15MW wind turbine for oscillation frequencies $f = \omega/(2\pi)$ of 0.01 Hz and 0.035 Hz.

The derivatives of the aerodynamic loads needed to evaluate the analytical expressions presented in section 2.4 are obtained using CCBlade, which is an efficient BEM solver with guaranteed convergence that evaluates the aerodynamic derivatives analytically [22]. For each reference turbine, the aerodynamic loads and their derivatives are evaluated for 60 wind speeds ranging from cut-in to cut-out wind speeds. The coefficients are then evaluated for 96 frequencies ranging from 0.005 to 0.1 Hz, with a step of 0.001 Hz.

Figure 4 shows a comparison of the surge aerodynamic damping coefficients evaluated by the three different methods for the three reference turbines. The color map and contour lines represent the aerodynamic damping and damping ratio, respectively, as a function of wind speed and oscillation frequency. The damping ratio is calculated relative to the critical damping based on the natural frequency at the mean position at each wind speed and the total inertia, including contributions from both the platform's mass and its zero frequency hydrodynamic added mass. The overall pattern is similar for the different methods and turbines, where a negative damping region is observed above rated wind speed and below the detuned blade pitch controller natural frequency f_{pc}. In this region, the blade pitch controller's response is fast enough to react to changes in relative wind speed caused by the nacelle motion, resulting in the infamous instability issue for FWTs [23, 24]. In the above-rated region, close estimates for the damping ratio are obtained from all methods. The CSD and analytical methods give somewhat larger damping ratios compared to those obtained from decay tests at low, below-rated, wind speeds. For near-rated wind speeds, both decay and CSD method give similar damping ratios. The analytical method gives damping ratios with a very steep variation with wind speed around the rated value, giving significantly larger values right below rated and smaller values right above rated compared to the other methods. This is due to unmodelled saturation effects and interaction between the blade pitch and generator torque controllers.

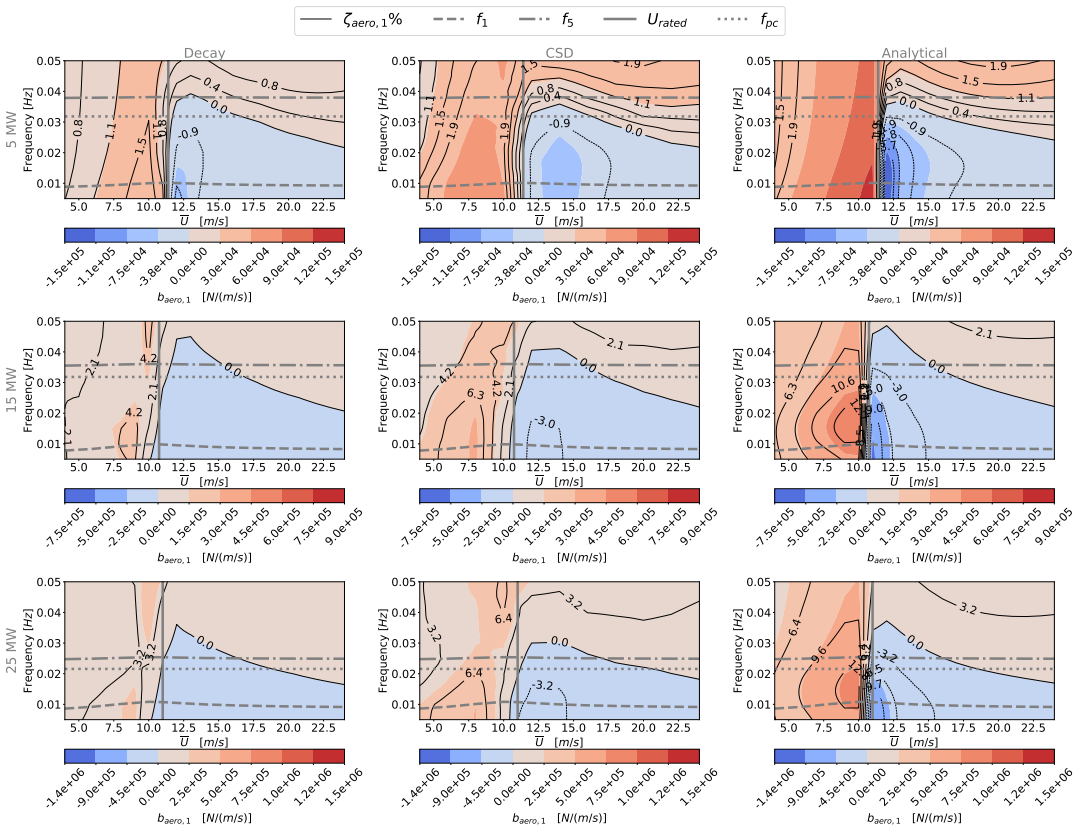

FIGURE 4 Surge aerodynamic damping coefficients. Each column contains plots for a different method, and each row contains plots for a different turbine size. Values on the black contours indicate surge damping ratio in %.

The aerodynamic pitch damping coefficients using the CSD method are found directly from the surge results, and are therefore not shown. Aerodynamic pitch damping coefficients for the three reference turbines from the decay and analytical methods are shown in Figure 5. The comparison between the estimates from the two methods is similar to that of surge damping. For the 5 MW turbine, which does not employ nacelle velocity feedback for blade pitch control, pitch damping has a similar pattern to surge damping. However, for the 15 and 25 MW turbines, the nacelle velocity feedback results in significant reduction in the negative damping region compared to the surge damping. This is because the blade pitch controllers of the 15 and 25 MW FWTs use the rotational nacelle velocity (equivalent to pitch velocity) as the feedback signal for blade pitch adjustment. It should be noted, however, that even if the translational nacelle velocity (which includes contributions from both surge and pitch velocities) is used as a feedback signal, the effect on surge damping might be insignificant due to the low velocities associated with the surge responses. This suggests that using aerodynamic surge damping to estimate aerodynamic pitch damping might result in inaccurate pitch response estimates when nacelle velocity feedback is utilized by the blade pitch controller.

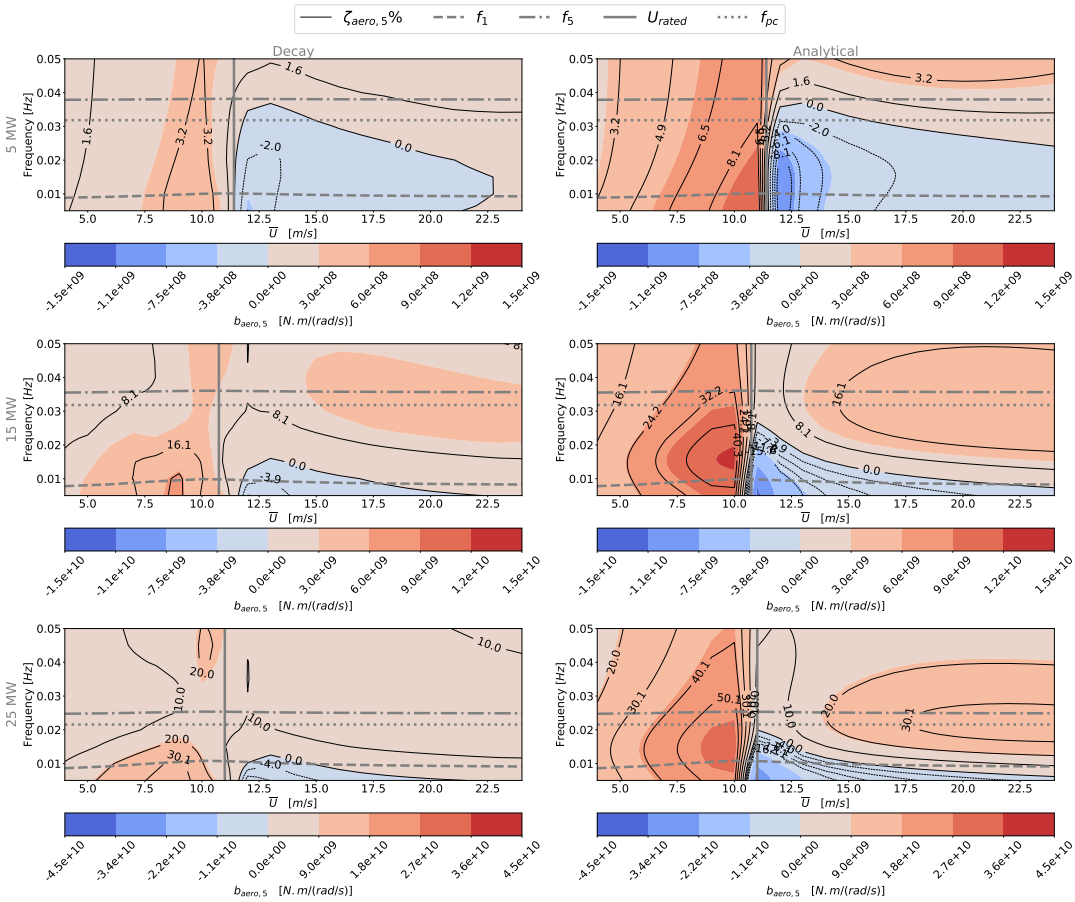

FIGURE 5 Pitch aerodynamic damping coefficients. Each column contains plots for a different method, and each row contains plots for a different turbine size. Values on the black contours indicate pitch damping ratio in %.

The different methods for evaluating aerodynamic added mass of surge and pitch for the 15 MW turbine are compared in Figures 6 and 7, respectively. The figures show color maps of the added mass coefficients in addition to contours showing how large the aerodynamic added mass is compared to the total (dry and hydrodynamic) mass or moment of inertia about the global pitch axis as defined in Figure 1 of the reference FWTs. For surge, the aerodynamic added mass values are small compared to the total inertia near the surge natural frequencies. On the other hand, the aerodynamic contribution to pitch inertia is significant for above-rated wind speeds, where the aerodynamic added inertia reaches around 40% of the total platform moment of inertia at the pitch natural frequency right above the rated wind speed as estimated by the decay and analytical approaches. The decay and analytical methods give close estimates for both the surge and pitch coefficients, although the variation of the coefficients is different near rated wind speed, especially for pitch. The pattern of variation of the pitch aerodynamic inertia obtained from the CSD approach is different compared to the other two methods and estimates a smaller contribution of aerodynamic inertia to the total inertia around rated wind speed. This, again, is because the CSD method does not account for nacelle velocity feedback effects on the blade pitch controller.

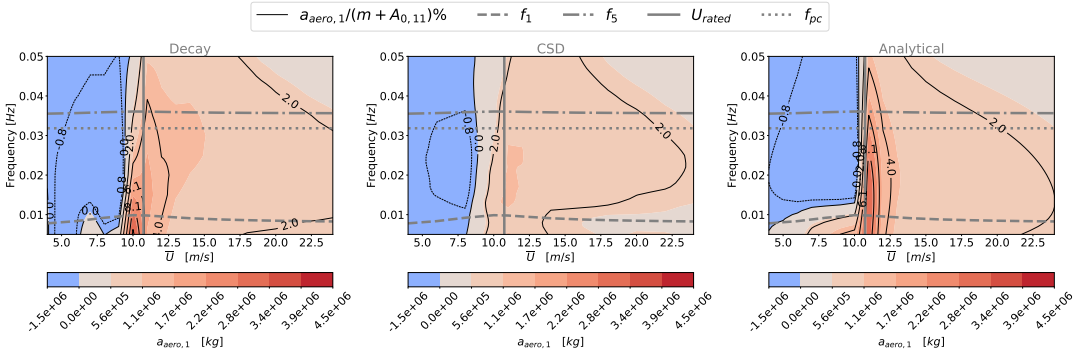

FIGURE 6 Comparison of surge aerodynamic added mass for the 15 MW wind turbine evaluated by three different methods. The values on the black contour lines indicate the ratio between the surge aerodynamic added mass and total FWT surge mass in %.

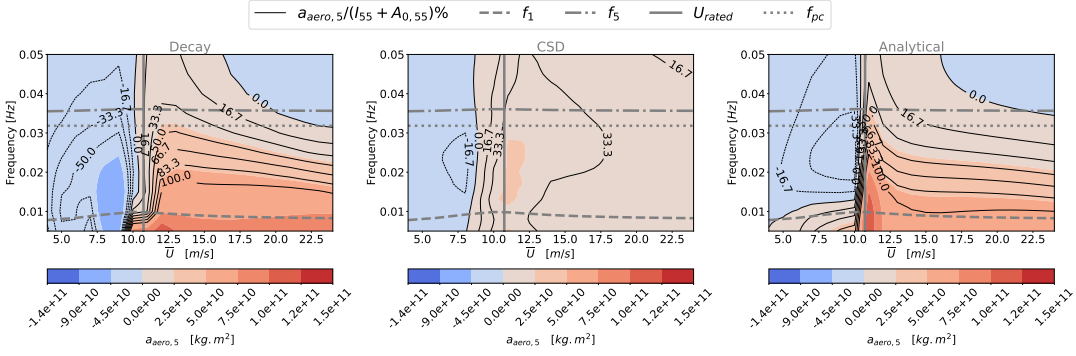

FIGURE 7 Comparison of pitch aerodynamic added mass for the 15 MW wind turbine evaluated by three different methods. The values on the black contour lines indicate the between the pitch aerodynamic added inertia and total FWT pitch inertia in %.

Two methods were used to obtain the transfer function for the aerodynamic excitation: 1) taking the square root of the ratio between the thrust PSD and rotor-averaged wind speed PSD and 2) the analytical expression in Equation (37). A comparison between the absolute value of the wind speed to thrust transfer function obtained by the two methods is given in Figure 8 for the 15 MW wind turbine (similar patterns are obtained for the other two reference turbines). Reasonable agreement between the two methods is found away from rated wind speed. Similar to damping, large differences between the two methods are found near rated wind speed where the analytical method overestimates the excitation force, which, as previously mentioned, can be attributed to the unmodelled saturation effects and the interaction between blade pitch and generator torque controllers.

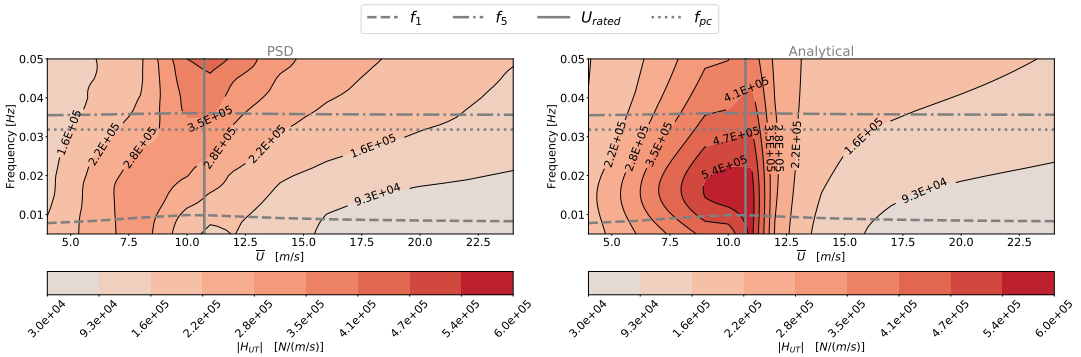

FIGURE 8 Comparison of surge aerodynamic wind to thrust gain for the 15MW wind turbine obtained from Equation (6) on the left and Equation (37) on the right.

The coefficients obtained from decay tests and analytical expressions experience large changes near rated wind speed due to the fact that they were obtained from steady wind simulations. Thus, to include the effect of the change of control region caused by turbulence, the coefficients are averaged based on a Gaussian distribution of the rotor-averaged wind speed around its mean value for the results shown in the next section. This improved the response predictions near rated wind speed.

3.2 | Response prediction

To evaluate the performance of the different modelling approaches presented in this work, comparisons between frequency-domain analyses and nonlinear coupled time-domain simulations were carried out. The coupled simulations were performed using OpenFAST for the three reference FWTs in turbulent wind conditions without waves. The wind conditions used for the coupled simulations of the FWTs are the same as those used for the fixed-nacelle simulations discussed in section 3.1, however, different random realizations of the wind fields are used for the floating case.

The aerodynamic coefficients presented in the previous section were used as lookup tables in frequency-domain analyses. A frequency-domain model of the FWTs was developed as a python package that derives the mass and hydrodynamic matrices required to solve Equation (1) from an OpenFAST model, which uses pre-generated hydrodynamic coefficients from a boundary element potential flow solver. In order to focus on the nonlinear damping effects associated with rotor dynamics, the linearized viscous damping matrix in Equation (1) ($\mathbf{B}_{lin}$) is set to be a diagonal matrix with 5% damping ratio for each DOF in both the frequency-domain model and the coupled time-domain simulations. The frequency-domain model uses the quasi-static mooring analysis python package MoorPy [25] to solve for the static equilibrium position of the FWT under the mean thrust for a given wind speed. Subsequently, the linearized mooring stiffness matrix at the mean position can be obtained from MoorPy based on a perturbation approach. Three

methods for modelling aero-servo dynamics were implemented in the frequency-domain analysis and are summarized in Table 2.

The standard deviations of surge and pitch estimated by the three methods for the three reference FWTs are compared against results from OpenFAST simulations in Figures 9 to 11. Both the mean and the range of variation of the standard deviations of the 6 time-domain realizations are shown. To demonstrate the effects of some of the modifications proposed in this work, the results from the decay test approach without the surge-pitch coupling terms and from the analytical expressions without the modifications proposed in Section 2.4 are also included in the comparison. All methods overpredict the surge response of the 5 MW FWT due to unmodelled mooring line damping in the frequency-domain analyses, which has a significant contribution to surge damping for this FWT. However, the surge response trend seems to be captured well by the decay and CSD approaches. For the below-rated wind speeds (4 to 10 m/s), the three proposed methods provide good estimates of the response statistics for both surge and pitch across all FWT sizes. Including the effects of the variation of the reference generator speed in the analytical expressions improves the estimates in the below-rated region.

In the above-rated wind speed region, only the decay test approach captures the trends of the time-domain results for both surge and pitch and for all FWTs. The CSD approach gives reasonable estimates for surge for all FWTs, however, it overpredicts pitch for above-rated wind speeds for the 15 and 25 MW FWTs. This overprediction is due to the fact that the nacelle velocity feedback effects cannot be captured by the CSD approach, since the aerodynamic coefficients are extracted from fixed nacelle simulations. Nevertheless, good estimates for pitch were still achieved for the 5 MW FWT which does not employ nacelle velocity feedback for blade pitch control. The analytical expressions result in large errors of surge and pitch estimates near the rated wind speed (11 to 14 m/s), which is likely due to the unmodelled saturation effects and interaction between the blade pitch and generator torque controllers around this region. For higher wind speeds, the analytical method gives good surge and pitch estimates for the 5 MW FWT, while slightly underestimating the pitch responses of the 15 and 25 MW FWTs compared to the other methods.

TABLE 2 Summary of the methods used to evaluate aerodynamic coefficients

Method	Excitation	Added mass and damping	Notation
1	Fixed-nacelle in turbulent wind (PSD)	Decay test in steady wind	PSD-Decay
2	Fixed-nacelle in turbulent wind (PSD)	Fixed-nacelle in turbulent wind (CSD)	PSD-CSD
3	Analytical expressions based on steady state		Analytical

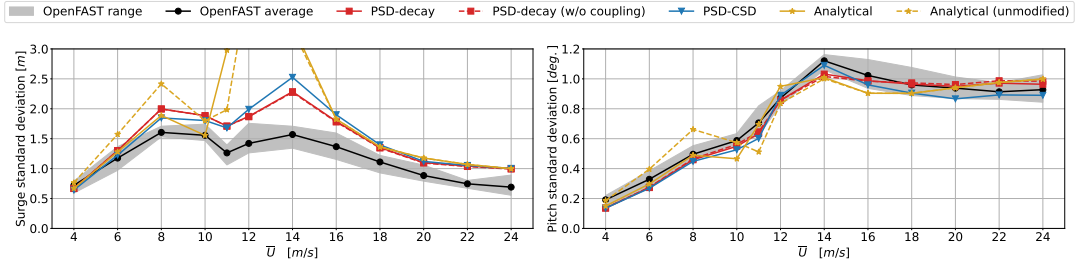

FIGURE 9 Comparison of response standard deviations for surge (left) and pitch (right) estimated from different methods for the 5 MW FWT.

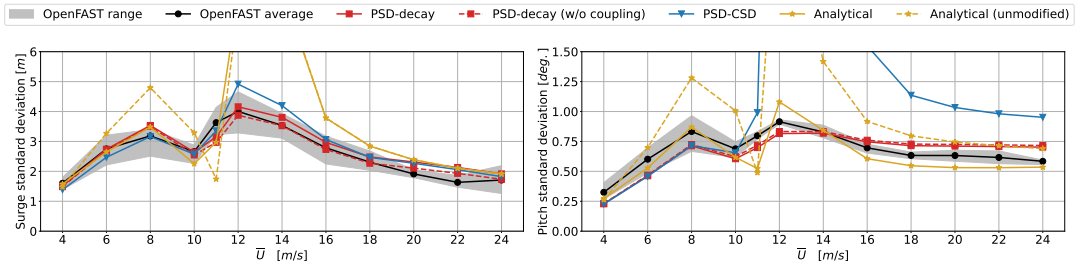

FIGURE 10 Comparison of response standard deviations for surge (left) and pitch (right) estimated from different methods for the 15 MW FWT.

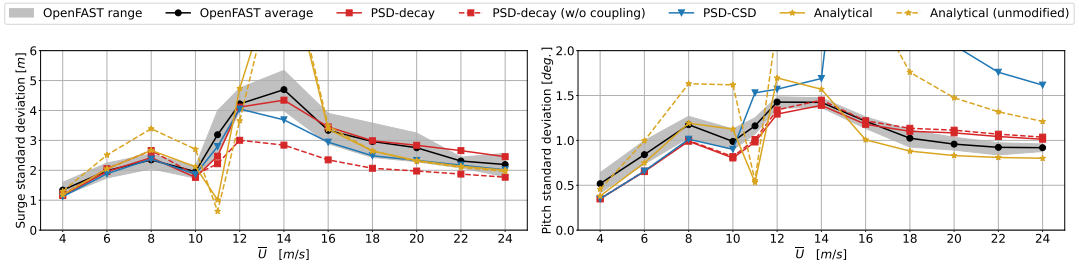

FIGURE 11 Comparison of response standard deviations for surge (left) and pitch (right) estimated from different methods for the 25 MW FWT.

Unlike the 5 and 15 MW FWTs, the effect of surge-pitch coupling is significant on the surge motion for above-rated wind speeds of the 25 MW FWT as shown in Figure 11. This is because of the low natural frequency of pitch of the 25 MW FWT, which becomes even lower due to the inertial effects of the blade pitch controller at above-rated wind speeds, resulting in pitch resonance occurring very close to surge natural frequency. This is further demonstrated in Figures 12 to 14 which show examples of surge and pitch PSDs for three mean wind speeds (4, 12, and 20 m/)s for the three reference FWTs. The natural frequencies of surge (f_1) and pitch (f_5) at the mean FWT position for each wind speed are highlighted. As indicated by the coefficients presented in the previous subsection, the inertial effects of the aero-servo dynamics of the turbines are only significant for pitch motion. This is illustrated by the apparent shift of pitch resonance from the pitch natural frequency calculated from solving the eigenvalue problem based on Equation (1) but without the aerodynamic effects. For the 25 MW FWT, this reduction in the pitch natural frequency results in thrust variations occurring at the surge natural frequency, thus exciting surge resonance. All three methods seem to capture this effect well for above-rated speeds for the 5 MW FWT, while only the decay test provide a close match to the results obtained from OpenFAST simulations for the 15 and 25 MW FWTs. Although the analytical approach underestimates the pitch response near resonance, it still captures the inertial effect relatively well. It is reemphasized here that the very large pitch response estimated by the CSD approach is caused by the effect of the nacelle velocity feedback on the blade pitch controller, which is only used for the 15 and 25 MW controllers.

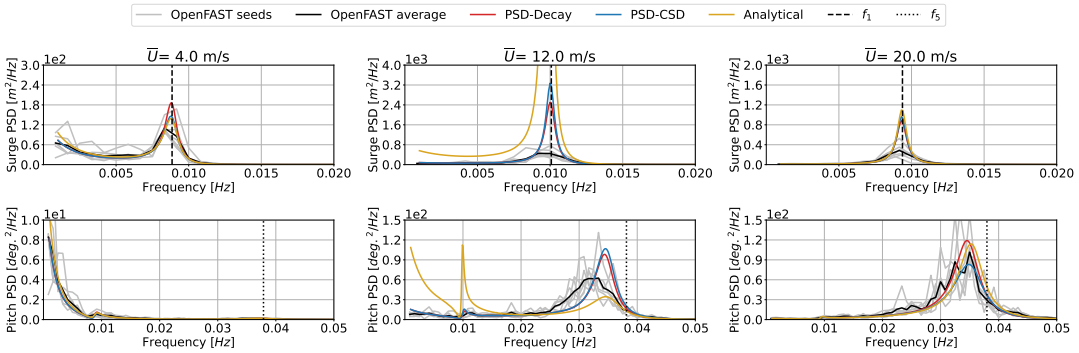

FIGURE 12 Comparison of response spectra for surge (upper row) and pitch (lower row) estimated from different methods for the 5 MW FWT at 3 wind speeds (4, 12, and 20 m/s). Vertical dashed and dotted lines highlight surge and pitch natural frequencies, respectively.

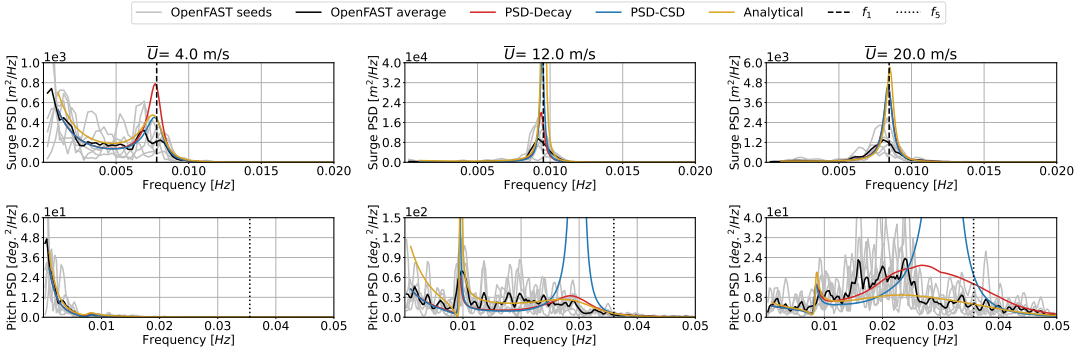

FIGURE 13 Comparison of response spectra for surge (upper row) and pitch (lower row) estimated from different methods for the 15 MW FWT at 3 wind speeds (4, 12, and 20 m/s). Vertical dashed and dotted lines highlight surge and pitch natural frequencies, respectively.

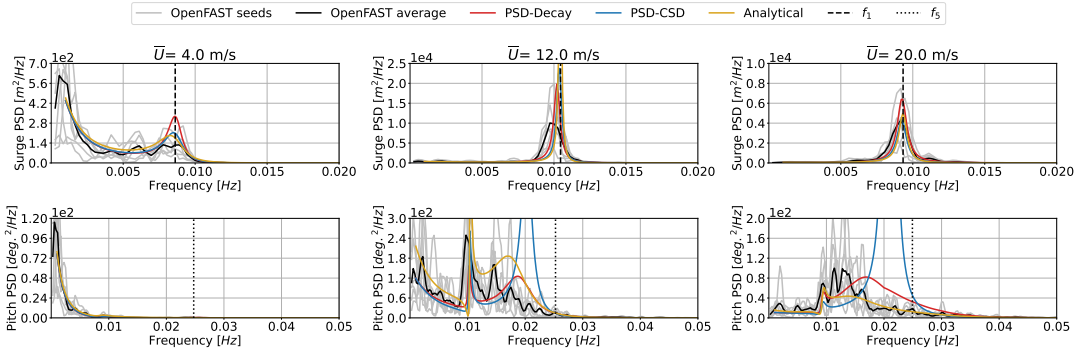

FIGURE 14 Comparison of response spectra for surge (upper row) and pitch (lower row) estimated from different methods for the 25 MW FWT at 3 wind speeds (4, 12, and 20 m/s). Vertical dashed and dotted lines highlight surge and pitch natural frequencies, respectively.

4 | CONCLUSIONS

This work explored different approaches to model the effects of the aerodynamic loads and controller action of the rotor on the low-frequency dynamics of FWTs in frequency-domain analyses. The main objective was to find a modelling approach that gives sufficiently accurate estimates of the wind-induced global motion responses of FWTs. This approach can then be used in a frequency-domain FWT model to optimize the floating support system components, such as the platform and mooring system, for given rotor and controller designs. The study focused on approaches that model rotor dynamics implicitly by introducing additional aerodynamic inertia, damping, and excitation coefficients to the equation of motion of the FWT.

Based on previous literature, three methods to evaluate the aerodynamic coefficients were investigated, and their limitations were addressed. The first method relies on coupled time-domain simulations in turbulent wind with a fixed nacelle and active rotor and controller DOFs, which have been used in previous studies to estimate aerodynamic excitation [4, 5, 6]. The method was extended to estimate aerodynamic added mass and damping from the CSD between rotor-averaged wind speed and thrust force by using turbulence as a proxy for nacelle motion. Secondly, the approach proposed by Pegalajar-Jurado et al. [6], which uses single DOF decay test simulations in steady wind, was generalized to provide the aerodynamic inertial effects and account for the frequency-dependence of the aerodynamic coefficients. This was achieved by tuning the natural frequency of the single DOF system of interest to different values covering a range of oscillating frequencies in which dynamic responses are expected. Finally, modifications to the analytical expressions of the aerodynamic coefficients, derived by Silva de Souza et al. [5] and later modified by Hall et al. [8], were proposed to account for the change in the generator torque controller reference speed in below-rated wind conditions and the filtering of the nacelle velocity feedback signal in above-rated wind conditions.

The three methods were evaluated through a case study of three reference FWTs with power ratings 5, 15, and 25 MW. The FWTs were simulated in turbulent wind conditions without waves using the coupled time-domain analysis tool OpenFAST and the surge and pitch responses were compared to estimates from frequency-domain analysis using the proposed approaches. All approaches were able to estimate both surge and pitch responses in below-rated wind conditions. The only approach which was able to provide good estimates in all cases was using fixed nacelle simulations in turbulent wind to obtain aerodynamic excitation and decay tests in steady wind to obtain aerodynamic inertia and damping coefficients. The CSD approach gave reasonable estimates for surge in all cases but failed to accurately estimate pitch responses in above-rated wind conditions for the 15 and 25 MW which. This is because these two FWTs use nacelle velocity feedback to adjust the blade pitch in above-rated conditions and the CSD approach, being obtained from fixed nacelle simulations, does not account for this effect. The approach relying on analytical expressions of aerodynamic coefficients severely overestimates responses around rated wind speeds, but provides better estimates at higher wind speeds for both surge and pitch.

The present work only considered implicit rotor dynamics modelling approaches, semi-submersible FWTs with catenary mooring systems, and blade pitch controllers that were detuned to have a frequency that is lower than the FWT's pitch natural frequency. However, the methods are applicable beyond these cases, and further studies should assess if the same conclusions apply for other systems.

The recommendations from this study are summarized below:

- The decay test approach seems to be the most reliable approach for implicit modelling of rotor contributions to FWT dynamics. Consequently, it is suitable for designing FWT support system components for given rotor and controller designs.
- The CSD approach can offer a good alternative in cases where only surge response is of interest, or when nacelle velocity feedback is not utilized by the blade pitch controller. This makes it possible to obtain all the aerodynamic

coefficients from fixed nacelle simulations and reduces the number of coupled time-domain simulations needed to be performed prior to the frequency-domain analysis.

- The analytical expressions need modifications for near and above-rated wind speeds. These modifications include the effects of saturation and interaction between the generator torque and blade pitch controllers. This can potentially be achieved via statistical linearization by explicitly solving the rotor dynamics in frequency-domain analyses.

ACKNOWLEDGEMENTS

The research leading to these results has received funding from the Research Council of Norway through the ENERGIX program (grant 308839) and industry partners Equinor, AIBEL, Dr. Techn. Olav Olsen, GCE Node Service, and Energy Valley.

NOMENCLATURE

Matrices

$\mathbf{A}_0$	Zero frequency hydrodynamic added mass matrix
$\mathbf{A}_{aero}$	Aerodynamic added mass matrix
$\mathbf{B}_{aero}$	Aerodynamic damping matrix
$\mathbf{B}_{lin}$	Linearized viscous damping matrix
$\mathbf{H}_{F\eta}$	Load to response transfer functions matrix
$\mathbf{K}_{hs}$	Hydrostatic stiffness matrix
$\mathbf{K}_{m}$	Linearized mooring stiffness matrix
$\mathbf{M}$	Mass matrix

Vectors

$\mathbf{F}_{aero}$	Wind excitation vector
RAO	Complex response amplitude operators vector
$\mathbf{S}_{\eta\eta}$	Response spectra vector
$\mathbf{f}_{aero}$	Wind excitation per unit wind turbulence amplitude vector
η	Floating wind turbine degrees of freedom
σ	Response standard deviation vector

Scalars

$C_{p,max}$	Wind turbine maximum power coefficient
H_{XY}	Transfer function between two variables X and Y
J	Rotor and drive train moment of inertia about low speed generator shaft
N_g	Gear ratio
Q	Aerodynamic torque
S_{XX}	Power spectral density of a variable X
S_{XY}	Cross spectral density between two variables X and Y
T	Aerodynamic thrust
U	Rotor-averaged wind speed
$a_{aero,i}$	Aerodynamic added mass (or moment of inertia) of a single degree of freedom denoted by i
$b_{aero,i}$	Aerodynamic damping of a single degree of freedom denoted by i
h_{hub}	Hub height
i	Imaginary unit (also denotes a degree of freedom index as a subscript)
k_{ff}	Nacelle velocity floating feedback gain
$k_{I\beta}, k_{I\tau}$	PI controller integral gains for blade pitch angle and generator torque
$k_{P\beta}, k_{P\tau}$	PI controller proportional gains for blade pitch angle and generator torque
s	Laplace variable
t	time
v	Nacelle horizontal velocity
Ω	Rotor speed
β	Blade pitch angle
η_{gb}	Gear box efficiency
$\zeta_{aero,i}$	Damping ratio of a single degree of freedom denoted by i
λ	Tip speed ratio
ρ	Density

τ_g Wind turbine generator torque

ω Angular frequency

Notations

$\overline{X}$ Mean value of

$\hat{X}$ Fourier transform of X

$\tilde{X}$ Laplace transform of X

$\Re\{X\}$ Real value of X

$\Im\{X\}$ Imaginary value of X

δX Variation of X around its mean value

REFERENCES

[1] Bachynski EE, Thys M, Sauder T, Chabaud V, Sæther LO. Real-time hybrid model testing of a braceless semi-submersible wind turbine: Part II—Experimental results. In: International Conference on Offshore Mechanics and Arctic Engineering, vol. 49972 American Society of Mechanical Engineers; 2016. p. V006T09A040.

[2] Goupee AJ, Kimball RW, Dagher HJ. Experimental observations of active blade pitch and generator control influence on floating wind turbine response. Renewable Energy 2017;104:9–19.

[3] Silva de Souza CE, Bachynski EE. Changes in surge and pitch decay periods of floating wind turbines for varying wind speed. Ocean engineering 2019;180:223–237.

[4] Hegseth JM, Bachynski EE. A semi-analytical frequency domain model for efficient design evaluation of spar floating wind turbines. Marine Structures 2019;64:186–210.

[5] Silva de Souza CE, Hegseth JM, Bachynski EE. Frequency-Dependent Aerodynamic Damping and Inertia in Linearized Dynamic Analysis of Floating Wind Turbines. Journal of Physics: Conference Series 2020;.

[6] Pegalajar-Jurado A, Borg M, Bredmose H. An efficient frequency-domain model for quick load analysis of floating offshore wind turbines. Wind Energy Science 2018;3(2):693–712.

[7] Bachynski EE. Design and dynamic analysis of tension leg platform wind turbines. PhD thesis, Norges teknisk-naturvitenskapelige universitet, Fakultet for …; 2014.

[8] Hall M, Housner S, Zalkind D, Bortolotti P, Ogden D, Barter G. An open-source frequency-domain model for floating wind turbine design optimization. In: Journal of physics: conference series, vol. 2265 IOP Publishing; 2022. p. 042020.

[9] Lupton RC, Langley RS. Improved linearised models of wind turbine aerodynamics and control system dynamics using harmonic linearisation. Renewable energy 2019;135:148–162.

[10] Lupton RC, Langley RS. Harmonic linearisation of aerodynamic loads in a frequency-domain model of a floating wind turbine. Wind Energy 2021;24(8):833–856.

[11] Da Silva LSP, Cazzolato BS, Sergiienko NY, Ding B. Efficient estimation of the nonlinear aerodynamic loads of floating offshore wind turbines under random waves and wind in frequency domain. Journal of Ocean Engineering and Marine Energy 2021;7(3):287–303.

[12] Da Silva LSP, de Oliveira M, Cazzolato B, Sergiienko N, Amaral G, Ding B. Statistical linearisation of a nonlinear floating offshore wind turbine under random waves and winds. Ocean Engineering 2022;261:112033.

[13] Abdelmoteleb SE, Mendoza ASE, dos Santos CR, Bachynski-Polić EE, Griffith DT, Oggiano L. Preliminary sizing and optimization of semisubmersible substructures for future generation offshore wind turbines. In: Journal of Physics: Conference Series, vol. 2362 IOP Publishing; 2022. p. 012001.

[14] Abbas N, Zalkind D, Pao L, Wright A. A Reference Open-Source Controller for Fixed and Floating Offshore Wind Turbines. Wind Energy Science Discussions 2021;2021:1–33. https://wes.copernicus.org/preprints/wes-2021-19/.

[15] Robertson A, Jonkman J, Masciola M, Song H, Goupee A, Coulling A, et al. Definition of the semisubmersible floating system for phase II of OC4. National Renewable Energy Lab.(NREL), Golden, CO (United States); 2014.

[16] Jonkman J, Butterfield S, Musial W, Scott G. Definition of a 5-MW reference wind turbine for offshore system development. National Renewable Energy Lab.(NREL), Golden, CO (United States); 2009.

[17] Allen C, Viscelli A, Dagher H, Goupee A, Gaertner E, Abbas N, et al. Definition of the UMaine VolturnUS-S reference platform developed for the IEA wind 15-megawatt offshore reference wind turbine. National Renewable Energy Lab.(NREL), Golden, CO (United States); Univ. of ...; 2020.

[18] Gaertner E, Rinker J, Sethuraman L, Zahle F, Anderson B, Barter GE, et al. IEA wind TCP task 37: definition of the IEA 15-megawatt offshore reference wind turbine. National Renewable Energy Lab.(NREL), Golden, CO (United States); 2020.

[19] OpenFAST, OpenFAST on GitHub; 2022. https://github.com/OpenFAST/openfast, accessed: Mar 2, 2022.

[20] Ning S. CCBlade Documentation: Release 0.1. 0. National Renewable Energy Lab.(NREL), Golden, CO (United States); 2013.

[21] Jonkman B. Turbsim user's guide v2. 00.00. Natl Renew Energy Lab 2014;.

[22] Ning SA. A simple solution method for the blade element momentum equations with guaranteed convergence. Wind Energy 2014;17(9):1327–1345.

[23] Larsen TJ, Hanson TD. A method to avoid negative damped low frequent tower vibrations for a floating, pitch controlled wind turbine. In: Journal of Physics: Conference Series, vol. 75 IOP Publishing; 2007. p. 012073.

[24] Jonkman J. Influence of control on the pitch damping of a floating wind turbine. In: 46th AIAA aerospace sciences meeting and exhibit; 2008. p. 1306.

[25] Hall M, Housner S, Sirnivas S, Wilson S, MoorPy (Quasi-Static Mooring Analysis in Python); 2021. https://doi.org/10.11578/dc.20210726.1. [Computer Software].